AIP Advances

Engineering helimagnetism in MnSi thin films

Cite as: AIP Advances **6**, 015217 (2016); https://doi.org/10.1063/1.4941316
Submitted: 22 November 2015 . Accepted: 15 January 2016 . Published Online: 29 January 2016

S. L. Zhang, R. Chalasani, A. A. Baker, N.-J. Steinke, A. I. Figueroa, A. Kohn, G. van der Laan, and T. Hesjedal

View Online Export Citation CrossMark

ARTICLES YOU MAY BE INTERESTED IN

Imaging and manipulation of skyrmion lattice domains in Cu_2OSeO_3
Applied Physics Letters **109**, 192406 (2016); https://doi.org/10.1063/1.4967499

Room temperature skyrmion ground state stabilized through interlayer exchange coupling
Applied Physics Letters **106**, 242404 (2015); https://doi.org/10.1063/1.4922726

The design and verification of MuMax3
AIP Advances **4**, 107133 (2014); https://doi.org/10.1063/1.4899186

NEW AVS Quantum Science
A high impact interdisciplinary journal for ALL quantum science
ACCEPTING SUBMISSIONS

AIP Publishing

© 2016 Author(s).

Engineering helimagnetism in MnSi thin films

S. L. Zhang,[1] R. Chalasani,[2] A. A. Baker,[1,3] N.-J. Steinke,[4] A. I. Figueroa,[3] A. Kohn,[2] G. van der Laan,[3] and T. Hesjedal[1,a]
[1]*Department of Physics, Clarendon Laboratory, University of Oxford, Oxford, OX1 3PU, United Kingdom*
[2]*Department of Materials Science and Engineering, Tel Aviv University, Ramat Aviv 6997801, Tel Aviv, Israel*
[3]*Magnetic Spectroscopy Group, Diamond Light Source, Didcot, OX11 0DE, United Kingdom*
[4]*ISIS, Harwell Science and Innovation Campus, Didcot, Oxfordshire, OX11 0QX, United Kingdom*

(Received 22 November 2015; accepted 15 January 2016; published online 29 January 2016)

Magnetic skyrmion materials have the great advantage of a robust topological magnetic structure, which makes them stable against the superparamagnetic effect and therefore a candidate for the next-generation of spintronic memory devices. Bulk MnSi, with an ordering temperature of 29.5 K, is a typical skyrmion system with a propagation vector periodicity of ∼18 nm. One crucial prerequisite for any kind of application, however, is the observation and precise control of skyrmions in thin films at room-temperature. Strain in epitaxial MnSi thin films is known to raise the transition temperature to 43 K. Here we show, using magnetometry and x-ray spectroscopy, that the transition temperature can be raised further through proximity coupling to a ferromagnetic layer. Similarly, the external field required to stabilize the helimagnetic phase is lowered. Transmission electron microscopy with element-sensitive detection is used to explore the structural origin of ferromagnetism in these Mn-doped substrates. Our work suggests that an artificial pinning layer, not limited to the MnSi/Si system, may enable room temperature, zero-field skyrmion thin-film systems, thereby opening the door to device applications. © *2016 Author(s). All article content, except where otherwise noted, is licensed under a Creative Commons Attribution (CC BY) license (http://creativecommons.org/licenses/by/4.0/).* [http://dx.doi.org/10.1063/1.4941316]

I. INTRODUCTION

Magnetic skyrmions[1] are topologically stable, vortex-like magnetization states that form periodic, six-fold symmetric lattices (with periodicities of approximately 3-30 nm).[2,3] Since each skyrmion can be seen as an ultra-stable carrier of information, the crystal itself can be regarded as a high-density, non-volatile information matrix, overcoming the limitations set by the superparamagnetic limit.[4] Owing to the ultra-low current densities needed to manipulate them,[5] skyrmions have become the focus of novel magnetic memory and logic concepts.[6,7] The broken inversion symmetry of the spin-orbit coupling is the key condition for the appearance of the Dzyaloshinskii-Moriya interaction (DMI), which is the essential ingredient for the existence of skyrmions. Currently, there are two major types of materials that support magnetic skyrmions. First, skyrmions are found in non-centrosymmetric crystals which are governed by the DMI such as the cubic B20 helimagnetic transition metal silicides and germanides, MnSi,[2] FeGe,[8] and MnGe,[9] as well as new space group $P4_132$ materials.[10] Second, skyrmions are observed in thin films[4,11] or heterostructures in which the DMI is induced by the specific structural boundary conditions.[12–15] Though the structural DMI systems support room-temperature skyrmion bubbles, only crystalline DMI systems support extremely long-range ordered skyrmion lattices, which unlock novel physics, such as emergent electromagnetism, magnetic monopoles and a rich variety of phase transitions, which are promising candidate for

[a]Corresponding author: Thorsten.Hesjedal@physics.ox.ac.uk

 ©Author(s) 2016.

advanced applications. Therefore, increasing the magnetic ordering temperature and decreasing the skyrmion-stabilizing magnetic field is very important for the future applications of these materials.

MnSi is a weak itinerant, helically ordered ferromagnet with a magnetic bulk moment of $\mu_{bulk} = 0.39\ \mu_B/Mn$,[16] naturally occurring in interplanetary dust particles.[17] The bulk Curie temperature, T_C, is 29.5 K.[16] For skyrmion-based spintronic applications, thin film materials are pivotal.[18] High-quality thin film MnSi has been grown by molecular beam epitaxy (MBE) on Si(111).[19] Owing to the difference in lattice constants between MnSi and Si, the film is tensily strained in the plane, with the strain monotonically decreasing with film thickness.[20] The out-of-plane strain, on the other hand, is compressive and a nonmonotic function of film thickness.[20] As a result of strain in the film, T_C becomes a function of film thickness and increases over 10 nm up to 43 K.[20]

Currently, there are two fundamental issues that hamper the application of skyrmion-carrying materials systems. Firstly, the candidate materials should have an ordering temperature above room temperature. Secondly, the skyrmion phase has to be stabilized in zero applied field. However, these issues remain challenging as there are no reported B20-type helimagnetic materials with a T_C above room temperature, and an external field is always required to manipulate the helimagnetism and stabilize the skyrmion phase.[2] Utilizing coupling mechanisms in artificial magnetic heterostructures provides a flexible playground for engineering B20 systems, as well as manipulating their helimagnetism. Here, we investigate the magnetic and structural properties of MBE-grown MnSi thin films using magnetometry, x-ray spectroscopy, electron microscopy, and x-ray diffraction. We find ferromagnetism in the seed layer, which persists up to room temperature, and which results in proximity coupling with the MnSi layer above.

II. THIN FILM GROWTH

Epitaxial MnSi(111) thin films were grown on Si(111) substrates measuring $10 \times 12\ mm^2$ using MBE. The Balzers MBE system has a base pressure of 5×10^{-10} mbar and is equipped with electron beam evaporators and effusion cells. Flux control is achieved via cross-beam mass spectrometry. Prior to loading, the Si wafers were first degreased, followed by etching in hydrofluoric acid and oxidation by H_2O_2. Annealing at 990°C, and growing a Si buffer layer, leads to the 7×7 reconstruction, as confirmed by reflection high energy electron diffraction (RHEED). The sample is then cooled down to room temperature and ~3 monolayers of Mn were deposited before they are reacted with the Si surface at an elevated temperature of ~400°C. One monolayer (ML) corresponds to 7.82×10^{14} atoms/cm^2. This leads to the reactive formation of an epitaxial MnSi seed layer.[21] For thicker Mn films, the supply of Si from the bulk is becoming the limiting factor, leading to deep holes.[21] The MnSi layer has a $(\sqrt{30} \times \sqrt{30})R30°$ structure, as determined by RHEED. Growth of the MnSi layer proceeds by stoichiometric deposition of Mn and Si, with the substrate at 250°C, up to a thickness of ~500 Å without any signs of the formation of a secondary phase in x-ray diffraction (XRD). The thicknesses obtained by x-ray reflectometry and *in-situ* film thickness monitoring agree well.[22]

III. MAGNETOMETRY

A. Superconducting quantum interference device (SQUID) studies

First, the temperature-magnetic field (T-B) phase diagram (PD) is studied as a function of MnSi thickness using SQUID magnetometry.[23] A one-to-one correspondence of the magnetic PD has been established between, on the one hand, studies of bulk samples using small-angle neutron scattering[2] and Lorentz transmission electron microscopy (LTEM)[24] and, on the other hand, ac and dc magnetometry. The details of the magnetic structures existing inside of the PD boundaries for MnSi thin films are still controversial in the literature: whereas some authors report the existence of a disordered skyrmion phase,[18] others argue that the observed data can be explained by a uniform conical phase.[25] However, the details of the magnetic structures inside the PD are not the focus of this work, as they require a different characterization approach. Here, we focus on the film-thickness

dependence of the PD boundaries only, since these variations suggest similar changes inside of the PD boundaries, as has been observed in other B20 thin film systems.[8]

The upper boundary, H_{c2}, which defines the transition from conical to field-polarized (FP) state, can be defined as the field at which the magnetic susceptibility is zero and is obtained from magnetization-field (M-H) curves. A linear background signal (containing, among others, the diamagnetic contribution of the substrate) was subtracted before performing this analysis. The transition temperature, T_C, is obtained from M-T profiles measured in different applied fields. The samples were field cooled to 5 K from room temperature in a field of 2 T. M-T curves were measured during the warm-up, at fixed field values. For the helimagnetic-to-paramagnetic transition, T_C is defined by the temperature point where $d^2M/dT^2 = 0$.

The amalgamation of H_{c2} and T_C defines the general shape of the magnetic PD, and the in-plane PD is shown in Fig. 1. The films show easy-plane anisotropy, and T_C is between 38 K and 47 K, depending on the film thickness. The saturation magnetization M_S is (0.41 ± 0.03) μ_B/Mn, assuming that the film is phase-pure in the B20 phase. The phase boundaries have a similar shape, however, the boundary values vary systematically with film thickness. Note the out-of-plane PD exhibit the same general trends with film thickness. First, T_C decreases as the thickness increases. This is commonly recognized as a strain effect since as the film becomes thicker, it should release the overall strain and eventually approach the bulk value of 29.5 K. Second, H_{c2} increases with film thickness for both in-plane and out-of-plane applied fields. This is an unusual behavior and cannot be simply explained by magnetic anisotropy effects, which, for thinner films with their stronger easy-plane anisotropy, would favor a lower in-plane and a higher out-of-plane H_{c2}. This means that the thinner films are easier to unwind from the conical state to the FP state, possibly pointing towards the existence of an 'internal' pinning field. This pinning effect has the same strength regardless of the sample thickness. We interpret this phenomenon as a magnetic proximity effect between the B20 helimagnetic thin film and the underlying interfacial volume, consisting of the MnSi seed layer and the upper layers of the Si substrate, as will be shown in the following.

B. X-ray magnetic circular dichroism

X-ray absorption spectra (XAS) at the Mn $L_{2,3}$ edges were measured on beamline I10 (BLADE) at the Diamond Light Source, UK, using a 14 T superconducting magnet. XAS measurements were

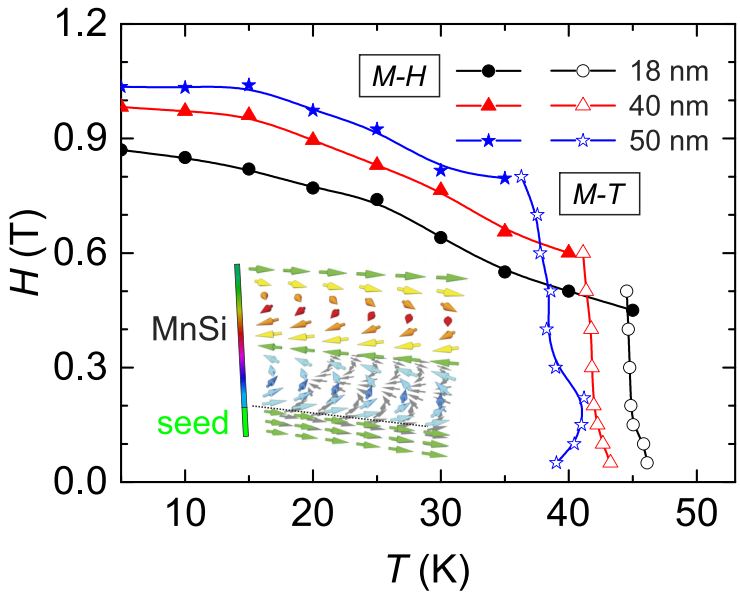

FIG. 1. Magnetic phase diagram of MnSi thin films. The phase boundaries of T_C (open symbols) and H_{c2} (solid symbols), within which the topologically non-trivial phase may exist, are shown as a function of film thickness. The field was applied in-plane. Inset: Model of the magnetic exchange biasing of the MnSi film due to the underlying seed layer.

made in total-electron-yield (TEY) and fluorescence-yield (FY) mode. Element-specific XMCD is used to probe the local electronic character of the magnetic ground state.[26] This technique allows for an unambiguous determination of the electronic and magnetic state of transition metals. XMCD is obtained from the difference between two XAS spectra recorded with the x-ray helicity vector and applied magnetic field parallel and antiparallel, respectively. The magnetic field is parallel to the x-ray beam which impinges at normal incidence. The XMCD is obtained by reversing the polarization of the incident x-rays to avoid having to change the magnetic field of the superconducting magnet.

At 40 K, i.e., a few degrees below the T_C of the 50-nm-thick MnSi film, the XMCD signal obtained in an applied field of 10 T shows ferromagnetic ordering both in surface-sensitive TEY [3-5 nm probing depth, see Fig. 2(a)] and bulk-sensitive FY mode [Fig. 2(b)]. The XMCD TEY spectrum shows the signature of Mn^{2+}.[27] The XMCD FY spectrum, on the other hand, suffers from strong saturation effects.[28] At 300 K, the surface-sensitive TEY signal has vanished (not shown), whereas the bulk-sensitive FY signal is still persistent [Fig. 2(c)]. An open-loop hysteresis curve is also seen in SQUID magnetization measurements [Fig. 2(d)]. This behavior clearly points towards room temperature ferromagnetic ordering in the seed layer region.

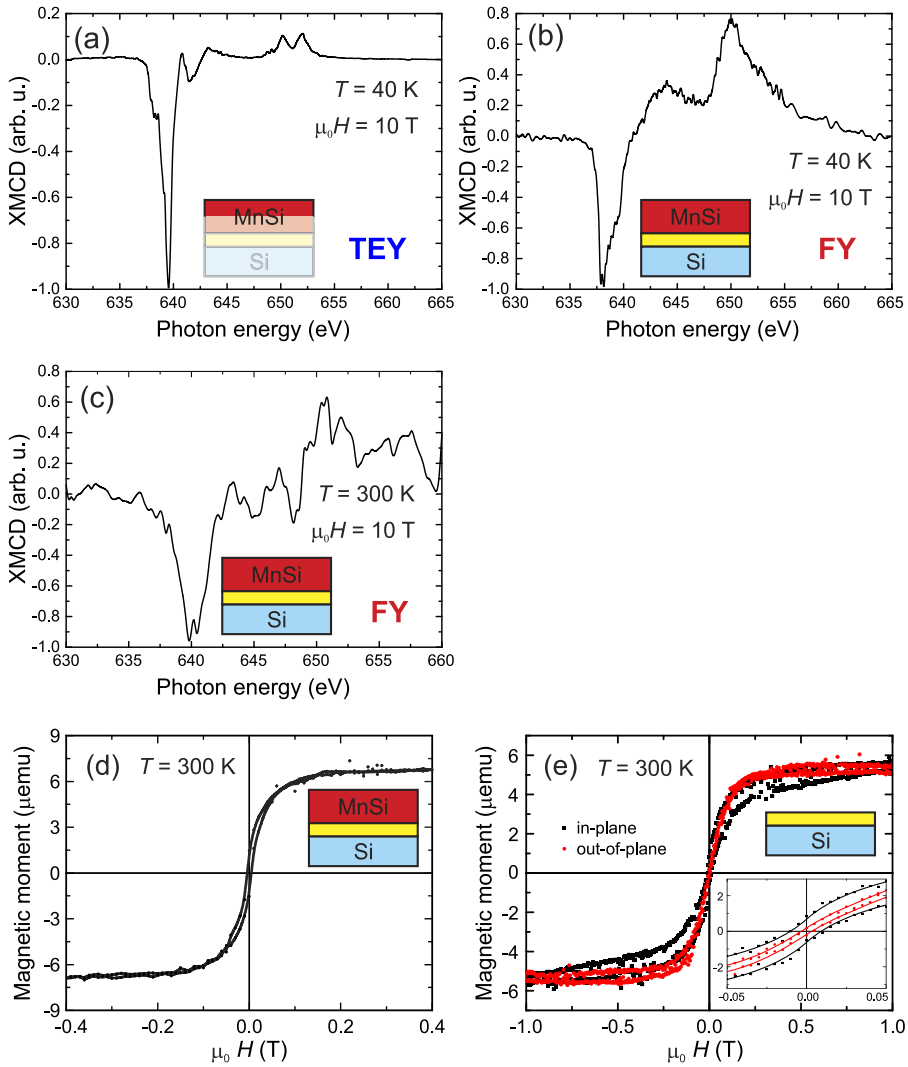

FIG. 2. XMCD spectra obtained on a 50-nm-thick MnSi film at 40 K (a,b) and 300 K (c), in TEY and FY mode as indicated. The probed sample volume is highlighted (the seed layer is shown in yellow). (d) SQUID magnetization curve of the MnSi thin film sample with the field applied in-plane measured at 300 K. The SQUID loops for a reactively grown seed layer measured with the field applied in-plane and out-of-plane at 300 K are shown in (e). The inset shows a close-up of the low-field region. The solid lines are guides to the eyes only.

The magnetization curves of a pure, reactively grown seed layer, shown in Fig. 2(e) with the field applied in-plane and out-of-plane, exhibit hysteretic behavior with a remanent magnetization [see inset in Fig. 2(e)], indicative of ferromagnetic ordering. Also, in-plane and out-of-plane magnetization curves are different, meaning that the observed ferromagnetism is not due to random magnetic clusters, but instead due to some long-range-ordered ferromagnetic phase showing magnetic anisotropy. In the following structural study, we try to shed light in the structural properties of the MnSi/Si interface region.

IV. STRUCTURAL AND COMPOSITIONAL ANALYSIS

A. High-resolution TEM of interface

High-resolution TEM (HRTEM, phase contrast) and scanning TEM (STEM) in high-angle annular dark-field mode (STEM-HAADF) was carried out on a JEOL JEM 2100F to study the structural properties of the interfacial region in greater detail. Selected area electron diffraction (SAED) was recorded using a Gatan Ultrascan 2k × 2k CCD. Electron energy-loss spectroscopy (EELS) was performed in energy-filtered TEM mode making use of a post-column Gatan QuantumSE GIF. The sample for TEM analysis was prepared by mechanical polishing and subsequent low energy Ar-ion milling.

Figure 3(a) shows a cross-sectional, bright-field TEM image of the MnSi/Si interface with a high-resolution (phase contrast) image as inset. The investigated film exhibits a low defect density. The SAED pattern of the film [Fig. 3(b)] is indexed with the cubic B20 MnSi phase (space group $P2_13$, a = 0.45564 nm) with a zone axis of [112]. The SAED pattern of the Si substrate [Fig. 3(c)]

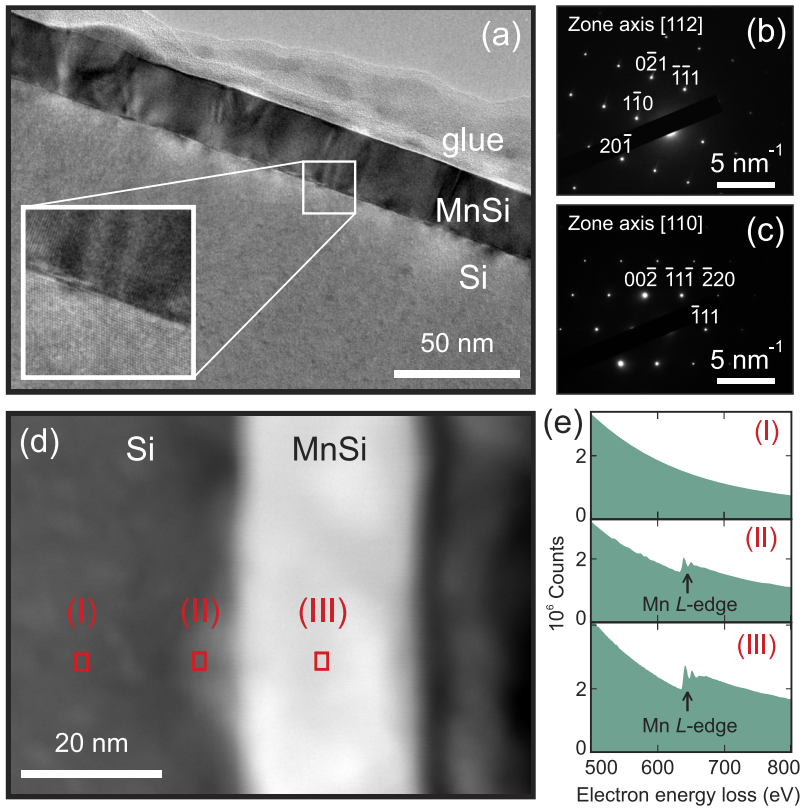

FIG. 3. (a) Bright-field TEM image of a MnSi film on a Si(111) substrate. SAED patterns of (b) the MnSi film and (c) the Si substrate. (d) Cross-sectional STEM-HAADF image of the MnSi/Si(111) interface. (e) The EELS spectra from the areas indicated by the red rectangles are shown at the right-hand side.

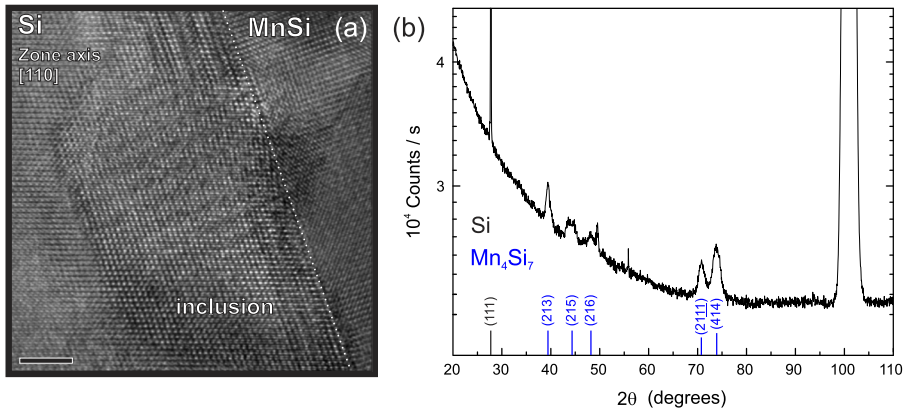

FIG. 4. (a) HRTEM image of the MnSi/Si interface showing an inclusion. The scale bar corresponds to 5 nm. (b) GIXRD diffraction pattern of the same sample, with Si and Mn_4Si_7 peaks labeled.

is indexed with the diamond space group $Fd\bar{3}m$ and the zone axis is identified as [110]. The SAED patterns of the interface also indicate that the $(\bar{1}\bar{1}1)$ planes of MnSi and the $(\bar{1}1\bar{1})$ planes of the Si substrate are parallel. From these observations, it can be concluded that the epitaxial relationship between the MnSi film and the Si substrate is MnSi{111}<112 >|| Si{111}<110>, as expected.[20]

To investigate the Mn diffusion into the Si(111) substrate, we used EELS spectra obtained in STEM mode with a probe size of about 1 nm in diameter. The STEM-HAADF Z-contrast image [Fig. 3(d)] clearly shows the uniform MnSi film, as well as a zone of local interface reaction with the Si(111) substrate. Point analysis was performed at several locations and the corresponding EELS spectra are shown on the right-hand side of Fig. 3(d). The spectra from the MnSi film (III) and the substrate close to the interface (II) show a signal at 640 eV, corresponding to Mn L edge, whereas Si far away from the interface (I) does not show a Mn signal. This measurement confirms that Mn diffused into the Si substrate.

B. Investigation of the inclusions by HRTEM and GIXRD

To analyze the Mn reaction in greater detail we performed HRTEM and grazing-incidence x-ray diffraction (GIXRD) analysis. A cross-sectional HRTEM image of the MnSi/Si(111) interface region is shown in Fig. 4(a). It should be noted that only a minority of the Si substrate is affected by this strong Mn diffusion, leading to an inclusion measuring $\sim 12 \times 22$ nm^2. The x-ray reflectometry data can be fitted by only taking the B20 MnSi, a homogeneous MnSi seed layer, and the substrate into account.[22] To identify the phase formed at the interface, different reflections were separately masked and the corresponding image reconstructed by an inverse Fourier transform (not shown). The extracted d-spacing of 3.81 Å is not present in either MnSi or Si, and points towards the presence of Si-rich manganese silicides, such as Mn_4Si_7.

The GIXRD patterns were recorded on a Rigaku Smartlab diffractometer using Cu $K\alpha$ radiation (λ = 1.54 Å) and a scan rate of 0.5° min^{-1}, in a 2θ range of 10°-110° at incidence angles between 0.25° and 2.75°, aligning with an arbitrary direction avoiding major reflections from both Si and MnSi. GIXRD reveals multiple peaks which are consistent with the formation of polycrystalline Mn_4Si_7 [cf. Fig. 4(b), incident angle 0.5°], however, we cannot rule out the possibility of more than one Mn_xSi_y phase within the seed layer. Nevertheless, GIXRD confirms the existence of additional phases below the ordered B20 MnSi layer, consistent with results of the magnetic and structural studies reported here.

V. DISCUSSION

In order to identify the source of the magnetic properties at the interface, one has to look at the magnetic properties of the structural entities present. Single crystals of Mn_4Si_7 show a $T_C \approx 40$ K,[29]

however, nanoinclusions in Si exhibit size-dependent ferromagnetic behavior up to 320 K (Ref. 30) due to stoichiometry, strain, charge accumulation, and interfacial magnetism.[31] The intrinsic mechanism leading to high-temperature ferromagnetic order in Mn_4Si_7 is exchange coupling between unbound 3*d* orbitals of Mn defects, mediated by spin fluctuations which exist at temperatures far above the bulk T_C.[32] Another possibility is the ferromagnetic ordering at room temperature associated with slightly non-stoichiometric $Si_{1-x}Mn_x$ ($x \approx 0.51$-0.55).[33] Although we find no hints for this behavior either in magnetometry or TEM, it cannot be fully excluded. In fact, deviations from the ideal stoichiometries could also be responsible for above room temperature ferromagnetism at interfaces between Mn and Si films[34] and around inclusions.[31] Previous studies on Mn-implanted Si have found above-room temperature ferromagnetism,[35] without the formation of Mn clusters,[36] and a tendency for Mn to diffuse to the surface.[37] X-ray-absorption studies show that Mn is neither incorporated substitutionally nor interstitially in the Si lattice, and the detailed doping scenario depends on the preparation conditions.[38]

Independent of the precise cause of the ferromagnetism, it is clear from the magnetometry data in Fig. 2(e) that the interface is ferromagnetically ordered, has an easy-plane anisotropy, and saturates at lower fields than the B20 MnSi. As the ferromagnetic layer is in contact with the helimagnetic layer, proximity coupling seems to exist, as illustrated in the inset to Fig. 1. For thinner films, the pinning is dominant, whereas for thicker films, the intrinsic properties of bulk B20 MnSi start taking over. Therefore, the interface can be regarded as a magnetic pinning layer that provides an effective 'internal field'. This internal field assists the unwinding of the conical state, transitioning into the FP state as observed in Fig. 1. From the presented data it is clear that this effect can be used to optimize and engineer the skyrmion phase, potentially allowing for its stabilization at zero applied field and higher T_C.

VI. SUMMARY AND CONCLUSIONS

In conclusion, we have shown that MnSi films grown on Si(111) experience proximity coupling to a ferromagnetic layer located at the interface between MnSi and Si using XMCD, magnetometry, and TEM. We have demonstrated an effective method to modify the phase diagram of MnSi thin films, utilizing the interlayer exchange interaction. In this case, one requires less external field to stabilize the helimagnetic phase and T_C can be significantly increased. We would like to emphasize that this method is not limited to MnSi/Si, but also applies to other B20 helimagnetic systems. One promising application for this approach is FeGe that has a higher, near-room temperature T_C. By fabricating an artificial pinning layer, such as NiFe, one may eventually realize room temperature, zero-field skyrmion thin film systems.

ACKNOWLEDGMENTS

This publication arises from research funded by the John Fell Oxford University Press (OUP) Research Fund. S. Z. acknowledges SRC for support and R. C. the Israel PBC fellowship. A. K. acknowledges the support of the Israel Science Foundation (grant 1321/13). The Diamond Light Source (UK) is acknowledged for beamtime (SI-9234) on I10.

[1] U. K. Rößler, A. N. Bogdanov, and C. Pfleiderer, Nature **442**, 797 (2006).
[2] S. Mühlbauer, B. Binz, F. Jonietz, C. Pfleiderer, A. Rosch, A. Neubauer, R. Georgii, and P. Böni, Science **323**, 915 (2009).
[3] C. Pfleiderer, T. Adams, A. Bauer, W. Biberacher, B. Binz, F. Birkelbach, P. Böni, C. Franz, R. Georgii, M. Janoschek, F. Jonietz, T. Keller, R. Ritz, S. Mühlbauer, W. Münzer, A. Neubauer, B. Pedersen, and A. Rosch, J. Phys.: Condens. Matter **22**, 164207 (2010).
[4] N. Romming, C. Hanneken, M. Menzel, J. E. Bickel, B. Wolter, K. von Bergmann, A. Kubetzka, and R. Wiesendanger, Science **341**, 636 (2013).
[5] F. Jonietz, S. Mühlbauer, C. Pfleiderer, A. Neubauer, W. Münzer, A. Bauer, T. Adams, R. Georgii, P. Böni, R. A. Duine, K. Everschor, M. Garst, and A. Rosch, Science **330**, 1648 (2010).
[6] A. Fert, V. Cros, and J. Sampaio, Nat. Nanotechnol. **8**, 152 (2013).
[7] S. Zhang, A. A. Baker, S. Komineas, and T. Hesjedal, Sci. Rep. **5**, 15773 (2015).
[8] X. Z. Yu, N. Kanazawa, Y. Onose, K. Kimoto, W. Z. Zhang, S. Ishiwata, Y. Matsui, and Y. Tokura, Nat. Mater. **10**, 106 (2011).

[9] N. Kanazawa, J. H. Kim, D. S. Inosov, J. S. White, N. Egetenmeyer, J. L. Gavilano, S. Ishiwata, Y. Onose, T. Arima, B. Keimer, and Y. Tokura, Phys. Rev. B **86**, 134425 (2012).
[10] Y. Tokunaga, X. Z. Yu, J. S. White, H. M. Rønnow, D. Morikawa, Y. Taguchi, and Y. Tokura, Nat. Commun. **6**, 7638 (2015).
[11] S. Heinze, K. von Bergmann, M. Menze, J. Brede, A. Kubetzka, R. Wiesendanger, G. Bihlmayer, and S. Blügel, Nat. Phys. **7**, 713 (2011).
[12] J. Li, A. Tan, K. W. Moon, A. Doran, M. A. Marcus, A. T. Young, E. Arenholz, S. Ma, R. F. Yang, C. Hwang, and Z. Q. Qiu, Nat. Commun. **5**, 4704 (2014).
[13] B. F. Miao, L. Sun, Y. W. Wu, X. D. Tao, X. Xiong, Y. Wen, R. X. Cao, P. Wang, D. Wu, Q. F. Zhan, B. You, J. Du, R. W. Li, and H. F. Ding, Phys. Rev. B **90**, 174411 (2014).
[14] D. A. Gilbert, B. B. Maranville, A. L. Balk, B. J. Kirby, P. Fischer, D. T. Pierce, J. Unguris, J. A. Borchers, and K. Liu, Nat. Commun. **6**, 8462 (2015).
[15] W. Jiang, P. Upadhyaya, W. Zhang, G. Yu, M. B. Jungfleisch, F. Y. Fradin, J. E. Pearson, Y. Tserkovnyak, K. L. Wang, O. Heinonen, S. G. E. te Velthuis, and A. Hoffmann, Science **349**, 283 (2015).
[16] D. Bloch, J. Voiron, V. Jaccarino, and J. H. Wernick, Phys. Lett. A **51**, 259 (1975).
[17] K. Nakamura-Messenger, L. P. Keller, S. J. Clemett, S. Messenger, J. H. Jones, R. L. Palma, R. O. Pepin, W. Kloeck, M. E. Zolensky, and H. Tatsuoka, Am. Mineral. **95**, 221 (2010).
[18] Y. Li, N. Kanazawa, X. Z. Yu, A. Tsukazaki, M. Kawasaki, M. Ichikawa, X. F. Jin, F. Kagawa, and Y. Tokura, Phys. Rev. Lett. **110**, 117202 (2013).
[19] E. Magnanoa, E. Carleschia, A. Nicolaoua, T. Pardinia, M. Zangrandoa, and F. Parmigiania, Surf. Sci. **600**, 3932 (2006).
[20] E. Karhu, S. Kahwaji, T. L. Monchesky, C. Parsons, M. D. Robertson, and C. Maunders, Phys. Rev. B **82**, 184417 (2010).
[21] S. Higashi, P. Kocan, and H. Tochihara, Phys. Rev. B **79**, 205312 (2009).
[22] B. Wiedemann, S. L. Zhang, Y. Khaydukov, T. Hesjedal, O. Soltwedel, T. Keller, S. Mühlbauer, A. Chacon, T. Adams, M. Halder, C. Pfleiderer, and P. Böni, Phys. Rev. B (2015) submitted.
[23] A. Bauer and C. Pfleiderer, Phys. Rev. B **85**, 214418 (2012).
[24] A. Tonomura, X. Yu, K. Yanagisawa, T. Matsuda, Y. Onose, N. Kanazawa, H. S. Park, and Y. Tokura, Nano Letters **12**, 1673 (2012).
[25] T. L. Monchesky, J. C. Loudon, M. D. Robertson, and A. N. Bogdanov, Phys. Rev. Lett. **112**, 059701 (2014).
[26] G. van der Laan, J. Phys.: Conf. Ser. **430**, 012127 (2013).
[27] G. van der Laan and B. T. Thole, Phys. Rev. B **43**, 13401 (1991).
[28] G. van der Laan and A. I. Figueroa, Coord. Chem. Rev. **277-278**, 95 (2014).
[29] A. Sulpice, U. Gottlieb, M. Affronte, and O. Laborde, J. Magn. Magn. Mater. **272–276**, 519 (2004).
[30] S. Zhou, A. Shalimov, K. Potzger, M. Helm, J. Fassbender, and H. Schmidt, Phys. Rev. B **80**, 174423 (2009).
[31] S. Yabuuchi, H. Kageshima, Y. Ono, M. Nagase, A. Fujiwara, and E. Ohta, Phys. Rev. B **78**, 045307 (2008).
[32] V. N. Men'shov, V. V. Tugushev, S. Caprara, and E. V. Chulkov, Phys. Rev. B **83**, 035201 (2011).
[33] V. V. Rylkov, A. S. Bugaev, O. A. Novodvorskii, V. V. Tugushev, E. T. Kulatov, A. V. Zenkevich, A. S. Semisalova, S. N. Nikolaev, A. S. Vedeneev, A. V. Shorokhova, D. V. Aver'yanov, K. Y. Chernoglazov, E. A. Gan'shina, A. B. Granovsky, Y. Wang, V. Y. Panchenko, and S. Zhou, J. Magn. Magn. Mater. **383**, 39 (2015).
[34] T. Takeuchi, Y. Hirayama, and M. Futamoto, IEEE Trans. Magn. **29**, 3090 (1993).
[35] M. Bolduc, C. Awo-Affouda, A. Stollenwerk, M. B. Huang, F. G. Ramos, G. Agnello, and V. P. LaBella, Phys. Rev. B **71**, 033302 (2005).
[36] P. R. Bandaru, J. Park, J. S. Lee, Y. J. Tang, L.-H. Chen, S. Jin, S. A. Song, and J. R. O'Brien, Appl. Phys. Lett. **89**, 112502 (2006).
[37] H. Francois-St-Cyr, E. Anoshkina, F. Stevie, L. Chow, K. Richardson, and D. Zhou, J. Vac. Sci. Technol. B **19**, 1769 (2001).
[38] A. Wolska, K. Lawniczak-Jablonska, M. Klepka, M. S. Walczak, and A. Misiuk, Phys. Rev. B **75**, 113201 (2007).